Notice: This manuscript has been authored by UT-Battelle, LLC, under contract DE-AC05-00OR22725 with the US Department of Energy (DOE). The US government retains and the publisher, by accepting the article for publication, acknowledges that the US government retains a nonexclusive, paid-up, irrevocable, worldwide license to publish or reproduce the published form of this manuscript, or allow others to do so, for US government purposes. DOE will provide public access to these results of federally sponsored research in accordance with the DOE Public Access Plan (http://energy.gov/downloads/doe-public-access-plan).

Magnetic Cations Doped into a Double Perovskite Semiconductor

Lun Jin, Danrui Ni, Xin Gui, Daniel B. Straus, Qiang Zhang and Robert J. Cava**

L. Jin, D. Ni, X. Gui, D. B. Straus and R. J. Cava

Department of Chemistry, Princeton University, Princeton, NJ, 08544, USA

***** E-mails of corresponding authors: ljin@princeton.edu; rcava@princeton.edu

Q. Zhang

Neutron Scattering Division, Oak Ridge National Laboratory, Oak Ridge, TN, 37831, USA

Keywords: cation-ordered double perovskites, magnetic cation doping, magnetic semiconductors, antiferromagnetic coupling, tunable band gap

We report two solid solutions based on the magnetic ion doping of the double perovskite oxide Sr_2GaSbO_6: $Sr_2Ga_{1-x}Cr_xSbO_6$ ($0.1 \leq x \leq 0.4$) and $Sr_2Ga_{1-x}Fe_xSbO_6$ ($0.1 \leq x \leq 0.4$). All compositions crystallize in the same space group (*I*4/*m*) as their undoped parent phase Sr_2GaSbO_6, with the trivalent magnetic cations Cr^{3+} or Fe^{3+} partially substituting for non-magnetic Ga^{3+} in one of the B-cation sites. The Cr- and Fe-doped phases display dominant antiferromagnetic coupling among the dopant magnetic moments, and exhibit decreasing band gaps with increasing substitution level.

1. Introduction

Complex metal oxides have been of enduring interest to scientists in a wide range of disciplines since they can exhibit intriguing physical properties, ranging from 'simple' magnetic and electronic states to 'complicated' collective behavior such as ferroelectricity and magnetoresistance.[1,2] Magnetic semiconductors, as a classic example of collective behavior, are materials that exhibit equally useful magnetic and semiconducting properties by utilizing the spin and charge of electrons simultaneously.[3–9] These spintronic materials are one of the keen research foci in materials science as they have the potential to significantly enhance the performance of devices for next-generation information technology.[10–13] The perovskite family, as one of the largest and most tolerant structural types in complex metal oxides, serves an important role in material designing area.[14–16] The ease of tuning the strength and sign of metal-oxygen coupling interactions by modifying the unit cell contents and crystallographic structures makes perovskites perfect candidates for future applications.

An $A_2BB'O_6$ B-site-cation-ordered double perovskite in which magnetic transition metal cations are absent, but which exhibits a band gap in the semiconducting regime, can be a perfect parent phase for fabricating dilute magnetic semiconductors. Magnetic-cation doping can then be achieved by partially replacing one of the non-magnetic B-site-cations with selected magnetic transition metal centers, to introduce magnetism into the semiconducting system. The preparation of cation ordered double perovskites is often not as straightforward as their cation disordered analogs, because random mixtures are often preferred unless the cation ordering is driven by strong chemical factors, such as distinguished ionic radii and/or formal oxidation states.[17,18]

Sr_2GaSbO_6 meets all the above-mentioned criteria. Although the ionic radius of Ga^{3+} (0.76 Å) is almost identical to that of Sb^{5+} (0.74 Å), there are two units of charge difference between Ga^{3+} and

Sb^{5+}, which yields a complete B-site cation ordered double perovskite with rock-salt type Ga^{3+}-Sb^{5+} ordering. However, it is indicated in the literature that when the ionic radii of B-site cations are similar and that for charge differences of two between the ions, there is invariably a small degree of anti-site disorder present.[17,18] Our double perovskite host material, Sr_2GaSbO_6, is reported to crystallize in a tetragonal space group $I4/m$ ($a^0a^0c^-$)[19]. The reflections allowed by the ordering of B-site cations have the same extinction as those resulting from tilting of octahedra along the *c* axis for this space group, making it difficult to quantify the degree of anti-site disorder, but none is reported.[20,21] To introduce magnetism into this magnetically silent system, trivalent transition metal cations Cr^{3+} and Fe^{3+} were selected to partially substitute for the non-magnetic B-site-cation Ga^{3+}, as Sr_2CrSbO_6[22–25] and Sr_2FeSbO_6[26–28] are well-established compounds. Thus, in this study, we have fabricated the undoped double perovskite parent phase Sr_2GaSbO_6, plus two series of doped double perovskite phases $Sr_2Ga_{1-x}Cr_xSbO_6$ ($0.1 \leq x \leq 0.4$) and $Sr_2Ga_{1-x}Fe_xSbO_6$ ($0.1 \leq x \leq 0.4$), and fully characterized them from the structural, magnetic, and optical points of view. The Cr and Fe dopants, while tuning the band gap in the two series, both lead to dominant antiferromagnetic coupling among the dopant magnetic moments.

2. Experimental

Polycrystalline powder samples of the undoped parent phase Sr_2GaSbO_6 and its magnetic-ion doped phases $Sr_2Ga_{1-x}Cr_xSbO_6$ ($0.1 \leq x \leq 0.4$) and $Sr_2Ga_{1-x}Fe_xSbO_6$ ($0.1 \leq x \leq 0.4$) were prepared by traditional high-temperature ceramic synthesis on a 0.5 g scale. Large-scale samples (approximately 3 g) of Sr_2GaSbO_6 and the two 10%-doped phases $Sr_2Ga_{0.9}M_{0.1}SbO_6$ (M = Cr and Fe) were also prepared via the same approach and employed for powder neutron diffraction characterization. Suitable stoichiometric metal ratios of $SrCO_3$ (Alfa Aesar, 99.99%), La_2O_3 (Alfa Aesar, 99.99%, dried at 900 °C), Ga_2O_3 (Alfa Aesar, 99.999%), Sb_2O_5 (Alfa Aesar, 99.998%),

Cr_2O_3 (Alfa Aesar, 99.97%) and Fe_3O_4 (Alfa Aesar, 99.997%) were thoroughly ground together by using an agate mortar and pestle, and then transferred into an alumina crucible for calcination. These reaction mixtures were first heated to 1000 ℃ in air at a heating rate of 1 ℃/min and held overnight to decompose the carbonate, and then were annealed in air at 1300 – 1400 ℃ (cooling rate = 3 ℃/min, reaction temperature varies slightly with the doping level) for 3 periods of 72 hours with intermittent grindings between heating periods. Routine inspections were carried out by laboratory X-ray powder diffraction data collected at room temperature on a Bruker D8 FOCUS diffractometer (Cu Kα) over a 2θ range between 5° and 70° after each heating period. Once the target product phases are pure and homogeneous, laboratory XRD data with much better statistical significance, covering a 2θ range between 5° and 110°, were collected from each sample. Room-temperature time-of-flight (TOF) neutron powder diffraction data were collected at Oak Ridge National Laboratory's Spallation Neutron Source, POWGEN beamline, using neutron beam with a center wavelength of 0.8 Å. Detailed structural analysis was performed by the Rietveld method[29] using the GSAS-II program. The particle morphology of selected compositions was examined by using an FEI XL30 field-emission gun scanning electron microscope (SEM) equipped with an Oxford X-Max 20 energy-dispersive X-ray spectroscope (EDX) running on AZtec software.

The magnetization data were collected using the Quantum Design Physical Property Measurement System (PPMS) equipped with a vibrating sample magnetometer (VSM) accessory. Temperature-dependent magnetization (M) data were collected from finely ground powders under an applied external field (H) of 1000 Oe. The resulting magnetic susceptibility χ (defined as M (in emu)/H (in Oe)) was then plotted against temperature. Field-dependent isothermal magnetization data between H = 90000 Oe and –90000 Oe were collected at T = 300 K and 2 K and plotted against field.

The diffuse reflectance spectra were collected from the powder sample of each composition at ambient temperature on a Cary 5000i UV-VIS-NIR spectrometer equipped with an internal DRA-2500 integrating sphere. The data were converted from reflectance to pseudo absorbance via applying the Kubelka–Munk function, and band gaps were calculated from Tauc plots by using both direct and indirect equations.[30]

The band structures for were calculated for Sr_2GaSbO_6, Sr_2CrSbO_6 and Sr_2FeSbO_6 using the WIEN2k program. The full-potential linearized augmented plane wave (FP-LAPW) method with local orbitals was used.[31,32] The generalized gradient approximation was used for dealing with electron correlation.[33] Reciprocal space integrations were completed over a 6×6×4 Monkhorst-Pack *k*-point mesh.[34] Spin-orbit coupling (SOC) effects were only applied for the Sb atom. Spin-polarization was only employed for the Cr and Fe atoms. The structural and lattice parameters of Sr_2GaSbO_6[19], Sr_2CrSbO_6[23] and Sr_2FeSbO_6[26] were obtained from the literature. With these settings, the calculated total energy converged to less than 0.1 meV per atom.

3. Results and Discussion

3.1 Structural Characterization

Sr_2GaSbO_6 is a B-site cation ordered double perovskite consisting of alternating GaO_6 and SbO_6 octahedra in the rock-salt-type ordering scheme[19]. The Rietveld co-refinement of standard laboratory X-ray powder diffraction (XRD) data and TOF neutron powder diffraction data (NPD) collected from the fine grey Sr_2GaSbO_6 powder indicates that it can be indexed by a body centered tetragonal unit cell, with lattice parameters a = 5.54042(4) Å, c = 7.90283(4) Å (wR = 7.303%; GOF = 3.01), which is consistent with the data found in the literature[19]. Observed, calculated and difference plots from the Rietveld co-refinement of Sr_2GaSbO_6 (space group $I4/m$) against the neutron and X-ray powder diffraction data are shown in the Supporting Information (SI) Figure

S1, with the detailed structural information listed in Table S1. The neutron scattering lengths of the B site elements (Ga: 7.288 fm and Sb: 5.57 fm) are too close to quantify the site occupancies the two elements to a precision beyond what is already known.

Since Sr_2GaSbO_6 is a magnetically silent semiconductor, the substitution of the non-magnetic B-site cation Ga^{3+} by the trivalent magnetic cations Cr^{3+} and Fe^{3+} should introduce magnetism into the system. The success of the doping of the double perovskite host was illustrated not only by the color changes of the doped samples (pink Cr-doped sample and pale-yellow Fe-doped sample) compared to the grey color of the undoped parent Sr_2GaSbO_6 phase, but also by the shift of peaks in the lab XRD patterns. The detailed structural characterization of the two 10%-doped phases $Sr_2Ga_{0.9}M_{0.1}SbO_6$ (M = Cr /Fe) was performed by co-refining the time of flight (TOF) neutron and lab X-ray powder diffraction data collected at 300 K against the reported structural model of their parent phase Sr_2GaSbO_6[19], with the all-Ga^{3+} site replaced by a mixture of 90% Ga^{3+} and 10% Cr^{3+}/Fe^{3+}. These two co-refinements both converged smoothly and provided satisfactory agreement parameters (Cr-doped: *wR* = 8.398%, *GOF* = 3.43; Fe-doped: *wR* = 8.951%, *GOF* = 3.46). Observed, calculated and difference plots from the Rietveld refinements of $Sr_2Ga_{0.9}M_{0.1}SbO_6$ (M = Cr/Fe, space group *I*4/*m*) against neutron powder diffraction data collected at 300 K are shown in Figure 1a & b (while those from the refinements against lab XRD data can be found in Figure S2), with the detailed structural information presented in Table 1 & 2. The structural model of $Sr_2Ga_{0.9}M_{0.1}SbO_6$ (M = Cr/Fe), and the bonding environments within the polyhedra are depicted in Figure 1c. Selected bond lengths for these polyhedra are listed in Table S2. The neutron scattering lengths of the dopant elements are: Cr: 3.635 fm and Fe: 9.45 fm. These are not sufficiently different from those of Ga and Sb to reliably refine the site fractions. The nominal compositions were confirmed by EDX and no evidence for mixing the B-site cations was

observed from lab XRD, or in the magnetization data (section 3.2). The extent of anti-site disorder over the B-sites in the doped materials, if any is present, is too small to be quantified by our analysis. It may be of interest in future studies to quantify whether a very small amount of anti-site disorder is present in these materials.

The attempts of 10% Cr-for-Ga and Fe-for-Ga substitution while the B-site-cation-ordering is still conserved indicates that Sr_2GaSbO_6 is capable of forming a partial solid-solution with Sr_2CrSbO_6 and Sr_2FeSbO_6 while maintaining the B-site cation ordering. Thus investigations of the remainder of the phase diagrams of these two solid-solutions were carried out by the fabrication and testing of materials with 10% increments in doping levels. The Ga-Cr and Ga-Fe systems both exhibit an upper doping limit of around 40% M-for-Ga substitution in a tetragonal symmetry ordered double perovskite phase. For higher levels of doping the materials become cation-disordered perovskite solid solutions. The presence of the disordered phase is evidenced for example by the appearance of a pseudo-cubic peak in the middle of the tetragonal doublet around the 2θ position of 46° in the laboratory XRD patterns for $Sr_2Ga_{0.6}M_{0.4}SbO_6$ (M = Cr/Fe), marked by the asterisk in Figure 2a. Thus, for compositions $x \geq 0.4$ in the $Sr_2Ga_{1-x}M_xSbO_6$ series (M = Cr/Fe), the samples are not single pure phase representatives of the B-site cation ordered double perovskite - but also contain B-site cation disordered single perovskites. These disordered phases are not the subject of the current work.

To further illustrate the successful synthesis of the doped phases, lattice parameters were determined by Rietveld refinements of the laboratory XRD data, and the resulting lattice parameters *a*, *c* and cell volume *V* are plotted against the doping level *x* in $Sr_2Ga_{1-x}M_xSbO_6$ for each dopant in Figure 2b. They exhibit significant curvature with respect to the doping level *x* for both Cr and Fe series. In contrast to the fitted lines in the *a* and *V* plots, the change in lattice

parameter *c* appears to be discontinuous and the trendline is simply a visual guide rather than a fit to the data. The data for the end-members Sr_2CrSbO_6[25] and Sr_2FeSbO_6[27] extracted from the literature (data points plotted as closed circles) in general fall in line with the materials reported in this study.

Finally, scanning electron microscope (SEM) images (Figure S3) were obtained from selected compositions in the $Sr_2Ga_{1-x}M_xSbO_6$ series (M = Cr/Fe) to observe particle morphologies and sample homogeneity. Our doped materials are clearly homogeneous single phases with uniform micron scale morphologies. Energy-dispersive X-ray spectroscopic (EDX) analysis provided compositional results that coincide with the nominal ones within experimental uncertainties, again proving that the doping was successful.

3.2 Magnetic Characterization

The temperature-dependent and field-dependent magnetization data collected for each composition of the $Sr_2Ga_{1-x}M_xSbO_6$ series (M = Cr/Fe) are plotted as magnetic susceptibility χ (M/H) against temperature T and magnetic moment M against field H, respectively, in the Supporting Information (SI) Figures S4 – S11. In Figure 3, in order to directly analyze the influences on magnetic properties exerted by dopants within these two doped series, the magnetic susceptibility χ (M/H), corrected by a small temperature-independent term χ_0, is plotted against temperature T, hence the first derivatives are summarized in the embedded plot to show the deviation from typical Curie-Weiss behavior; and the magnetic moment M collected at 2 K is plotted against field H as well for each composition of the Cr- and Fe-doped $Sr_2Ga_{1-x}M_xSbO_6$ series. The deviation from linear behavior in the first derivative plots and the 2 K isotherms clearly indicate that magnetic couplings between spins get stronger and the systems become less magnetically saturated at higher dopant contents. Zero field splitting does not apply here, since

both high spin d^3 Cr^{3+} and d^5 Fe^{3+} (see below) have an orbitally singlet ground state ($^4A_{2g}$ and $^6A_{1g}$ in spectroscopic language, in an octahedral crystal field) for isolated cations. The magnetic susceptibility data, over the suitable temperature range (selected as the straight-line part of the 1/ χ vs T curves) of these doped phases were then fitted to the Curie-Weiss law ($\chi = C/(T - \theta) + \chi_0$), in which a set of values of Curie constant C and Weiss temperature θ that are extracted and listed in Table S3 and depicted in Figure 4a & b. The magnetization data for both end-members Sr_2CrSbO_6[23] and Sr_2FeSbO_6[25] are extracted from the literature (data points in red circles). Those data all fall in line with the materials reported in this study.

For all four Cr-doped double perovskite materials, $Sr_2Ga_{1-x}Cr_xSbO_6$ ($0.1 \leq x \leq 0.4$), the magnetic susceptibility data in the whole measured temperature range $1.8 \leq T / K \leq 300$ can be fitted to the Curie-Weiss law. The inverse of χ exhibits a perfect linear relationship with temperature T and the data extracted agrees with the frequently observed high-spin d^3 electronic configuration of Cr^{3+}. The Weiss temperature θ progresses from an approximately-zero value to a small negative value, which suggests that a weak antiferromagnetic coupling dominates upon elevating the doping level of Cr^{3+} (Figure 4). The isothermal magnetization data collected from the Cr-doped materials at 300 K as a function of applied field is linear and passes through the origin, with a small positive slope, while the analogous data collected at 2 K exhibit some 'S-shape' features with positive slopes as well, and does not exhibit any hysteresis, consistent with the temperature-dependent magnetization data. The 'S-shape' features in the 2 K isotherms become less significant and progressively approach a linear shape with increasing substitution level x (Figure 3).

The four Fe-doped double perovskites, $Sr_2Ga_{1-x}Fe_xSbO_6$ ($0.1 \leq x \leq 0.4$) exhibit similar bulk magnetic properties compared to their Cr analogs, but the inverse of χ exhibits a perfect linear relationship with temperature T within a smaller temperature range ($30 \leq T / K \leq 300$). The data

extracted are consistent with a high-spin d^5 electronic configuration for Fe^{3+}. The Weiss temperatures θ extracted are all negative and increase in magnitude upon increasing the doping level of Fe^{3+}, which suggests that antiferromagnetic couplings become much stronger with increasing *x* for $Sr_2Ga_{1-x}Fe_xSbO_6$ (Figure 4). The isothermal magnetization data collected from the Fe-doped phases at 300 K is linear as a function of applied field and passes through the origin, with a small positive slope; analogous data collected at 2 K have positive slopes as well and do not exhibit any hysteresis. The much more prominent 'S-shape' features observed in the 2 K isotherms of the Fe-doped phases compared to their Cr-doped analogs are consistent with the temperature-dependent magnetization data.

In Figure 4c, the observed effective moment per formula unit $\mu_{eff.obs}$ is plotted against the calculated effective moment per formula unit $\mu_{eff.cal}$ extracted based on the spin-only value of the transition metal magnetic moment. The trend lines align perfectly along the diagonal of the quadrant for both Cr and Fe cases, which means that the observed $\mu_{eff.obs}$ and theoretical $\mu_{eff.cal}$ completely coincide. This reflects the presence of neglectable orbital angular momentum contributions for magnetism in these two series. In Figure 4d, the observed magnetization M per formula unit collected at T = 2 K under an applied field of 9 T is plotted against the calculated saturation magnetization M_s per formula unit. For the Fe-doped double perovskite series, the observed magnetization M is almost independent of the Fe-doping concentration, and thus the trend line is nearly parallel to the *x*-axis. As a clear distinction from the Fe analogs, in the Cr-doped series the observed magnetization M increases with elevated doping level *x*, but the increments gradually reduce with respect to the 10% intervals in dopant concentrations.

3.3 Band Structures and Band Gaps

The band structures of the undoped parent phase Sr_2GaSbO_6 and two end-members Sr_2CrSbO_6 and Sr_2FeSbO_6 are calculated by the method described in the experimental section. For the undoped double perovskite Sr_2GaSbO_6 (Figure 5a), a direct bandgap is exhibited at the Γ point (~ 1 eV) while a much larger indirect one (~3 eV) is observed between the Γ and N points. A nearly flat band which sits almost on top of the Fermi level is calculated to exist between the Γ and X points. For both end-members Sr_2CrSbO_6 (Figure 5b) and Sr_2FeSbO_6 (Figure 5c), the spin structures for the calculations were set to be antiferromagnetic based on the data found in the literature[23,26]. Firstly, both calculations suggest that both Sr_2CrSbO_6 and Sr_2FeSbO_6 have significantly smaller bandgaps than non-magnetic Sr_2GaSbO_6. A direct small, calculated bandgap (~0.2 eV) emerges at the S point for Sr_2CrSbO_6, while a flat continuous bandgap (~0.1 eV) is observed between the Γ and Z points for Sr_2FeSbO_6. Secondly, Sr_2CrSbO_6 has a nearly flat band just below the Fermi level through the Brillouin zone, while Sr_2FeSbO_6 has one just above. Thus based on the calculation, electron-doping of Sr_2FeSbO_6, to push the Fermi level closer to the energy of the flat band may be of future interest.

To experimentally evaluate the bandgaps of the $Sr_2Ga_{1-x}M_xSbO_6$ series (M = Cr/Fe) prepared in this study, the diffuse reflectance spectra were collected from powder samples at ambient temperature. The pseudo-absorbance (transferred from the observed reflectance using the Kubelka-Munk function) is plotted against photon energy (eV) in Figure 6a & b. The optical band gaps of these phases were then analyzed by Tauc plots using both direct and indirect transition equations (Table S4). The band gap of the undoped double perovskite Sr_2GaSbO_6 host is calculated to be 3.83 eV via the direct-transition approach, while it is found to be 3.52 eV via the indirect one. Thus the pale grey appearance of the prepared Sr_2GaSbO_6 polycrystalline powders clearly agrees more with the experimental bandgaps obtained from the diffuse reflectance spectra than the

calculated ones obtained from the band structure calculations (from both the literature[35] and our own). This is not surprising as DFT calculations are known to underestimate band gaps for compounds containing main group elements.[36–40]

For consistency, the largest transition in each phase was taken to experimentally evaluate the resulting bandgap. Using that data, we found that the size of band gap decreases with increasing doping level *x* in both the Cr- and Fe-doped systems, and though generally similar, different-in-detail behavior is observed in the optical data for each doped series (Figure 6). The Cr- and Fe-doped phases have similar absorption behavior in the 3 to 4 eV range but are differentiated with some additional absorption features in the lower energy regime. In general, the Cr-doped phases have a more intense color than the Fe-doped ones, corresponding to more intense absorptions in the visible-light region, since *d-d* transitions are allowed for Cr^{3+} but not for Fe^{3+} in this case. The Cr-doped phases (pink color) display absorptions at around 1.6 eV and 2.4 eV as a consequence of a *d-d* transition, which gets stronger with more Cr^{3+} substitution (Figure 6a). This feature has been observed in many minerals containing octahedrally coordinated Cr^{3+}, and it is reported that there is a trend of increasing ligand field splitting energy Δ_o with decreasing metal-oxygen bond length *R* in approximate compliance with the relationship: $\Delta_o \propto 1/R^5$.[41] Thus, by comparing the Cr-O bond length in our materials to reported minerals, a value of ligand field splitting energy $\Delta_o \approx 2.3$ eV can be estimated. In contrast, Fe^{3+} is confirmed by magnetization data to have a high-spin d^5 electronic configuration, and thus in the Fe-doped series, all the *d-d* bands are expected to be spin forbidden and these transitions should therefore be weak. A small absorption does appear at around 2.6 eV in Figure 6b, however, and this absorption becomes stronger with increasing doping level *x*, consistent with the pale yellow appearance of the powder samples, for which the color becomes more intense upon elevated Fe^{3+} dopant concentration. This weak coloration can be

rationalized as being due to the weak spin-forbidden transitions or localized energy states in the band gap brought on as a consequence of doping. Similar absorption phenomena have been previously observed in other polycrystalline semiconductor materials[42,43]. The band gaps plotted in Figure 6c are all calculated from Tauc plots by using an indirect transition equation; these values will be larger if a direct transition equation is used instead (Table S4) although the trend remains the same. The only anomaly that does not fall in line in either series is $Sr_2Ga_{0.6}Cr_{0.4}SbO_6$, it has a larger bandgap than can be expected from a simple atomic substitution. Thus using either the direct or indirect approach, the band gaps measured by diffuse reflectance spectroscopy serve as strong evidence that the Cr- and Fe-doped $Sr_2Ga_{1-x}M_xSbO_6$ double perovskites are semiconductors with tunable band gaps.

4. Conclusions

The B-site cation ordered double perovskite Sr_2GaSbO_6 and its magnetic-cation doped phases $Sr_2Ga_{1-x}Cr_xSbO_6$ ($0.1 \leq x \leq 0.4$), $Sr_2Ga_{1-x}Fe_xSbO_6$ ($0.1 \leq x \leq 0.4$) were synthesized by a conventional solid state reaction method and studied from structural, magnetic and optical points of view. The doped materials crystallize in the same space group (*I*4/*m*) as their undoped parent phase Sr_2GaSbO_6, with the Ga^{3+}/M^{3+} cations completely ordered with Sb^{5+}. The upper doping limit was found to be 40% in both systems, as evidenced by the appearance of a pseudo-cubic peak in the middle of the tetragonal doublet around the 2θ position of 46° in the laboratory XRD patterns, which represents the growth of B-site cation disordered perovskites. Magnetization data collected from the doped phases show that the Cr- and Fe-doped materials exhibit antiferromagnetic coupling among the dopant magnetic moments, which become stronger with increasing doping levels. The diffuse reflectance spectra collected indicate that the bandgap of the undoped parent phase Sr_2GaSbO_6 has been reduced upon Cr- or Fe-doping, and in general the bandgap shows a

decreasing trend with respect to the increasing doping level. It is not surprising, since according to our band structure calculations, both end members Sr_2CrSbO_6 and Sr_2FeSbO_6 have significant smaller bandgaps than Sr_2GaSbO_6. For comparison, as reported in one of our other studies, Mn dopants can introduce tunable ferromagnetism and bandgaps into the magnetically silent oxide double perovskite semiconductor as well.[44] Therefore, by selecting the appropriate magnetic dopant and controlling the doping level, magnetic semiconductors with desired physical properties can be fabricated.

Supporting Information

The Supporting Information is available from the Wiley Online Library or from the author.

Author contributions

Lun Jin: Methodology, Software, Formal analysis, Investigation, Data Curation, Writing - Original Draft, Visualization, Project administration.

Danrui Ni, Xin Gui, Daniel B. Straus and Qiang Zhang: Software, Investigation, Data Curation, Writing - Review & Editing.

Robert J. Cava: Conceptualization, Validation, Resources, Writing - Review & Editing, Supervision, Project administration, Funding acquisition.

Acknowledgements

This research was primarily done at Princeton University, supported by the US Department of Energy, Division of Basic Energy Sciences, grant number DE-FG02-98ER45706. A portion of this research used resources at the Spallation Neutron Source, a DOE Office of Science User Facility operated by the Oak Ridge National Laboratory. The authors acknowledge the use of Princeton's Imaging and Analysis Center, which is partially supported through the Princeton Center for Complex Materials (PCCM), a National Science Foundation (NSF)-MRSEC program (DMR-2011750).

Conflict of Interest

The authors declare no conflict of interest.

Table 1. Structural parameters and crystallographic positions from the co-refinement of neutron and X-ray powder diffraction data collected from $Sr_2Ga_{0.9}Cr_{0.1}SbO_6$ at 300 K.

Atoms	*x*/*a*	*y*/*b*	*z*/*c*	S.O.F.	U_{iso} equiv. (Å^2)
Sr1	0	0.5	0.25	1	0.00645
Ga1	0	0	0	0.9	0.00002
Sb1	0.5	0.5	0	1	0.00604
O1	0	0	0.2518(4)	1	0.01029
O2	0.2248(3)	0.2765(3)	0	1	0.00794
Cr1	0	0	0	0.1	0.00002

$Sr_2Ga_{0.9}Cr_{0.1}SbO_6$ space group *I*4/*m* (#87)
Formula weight: 460.95 g mol^{-1}, Z = 2
a = 5.54463(4) Å, *c* = 7.90344(4) Å, Volume = 242.975(3) Å^3
Radiation source: time of flight neutrons and Cu K-α
Temperature: 300 K
wR = 8.398%; *GOF* = 3.43

Table 2. Structural parameters and crystallographic positions from the co-refinement of neutron and X-ray powder diffraction data collected from $Sr_2Ga_{0.9}Fe_{0.1}SbO_6$ at 300 K.

Atoms	*x*/*a*	*y*/*b*	*z*/*c*	S.O.F.	U_{iso} equiv. (Å^2)
Sr1	0	0.5	0.25	1	0.00643
Ga1	0	0	0	0.9	0.00090
Sb1	0.5	0.5	0	1	0.00469
O1	0	0	0.2499(4)	1	0.00996
O2	0.2240(3)	0.2771(3)	0	1	0.00784
Fe1	0	0	0	0.1	0.00090

$Sr_2Ga_{0.9}Fe_{0.1}SbO_6$ space group *I*4/*m* (#87)
Formula weight: 461.33 g mol^{-1}, Z = 2
a = 5.54627(3) Å, *c* = 7.91029(3) Å, Volume = 243.330(3) Å^3
Radiation source: time of flight neutrons and Cu K-α
Temperature: 300 K
wR = 8.951%; *GOF* = 3.46

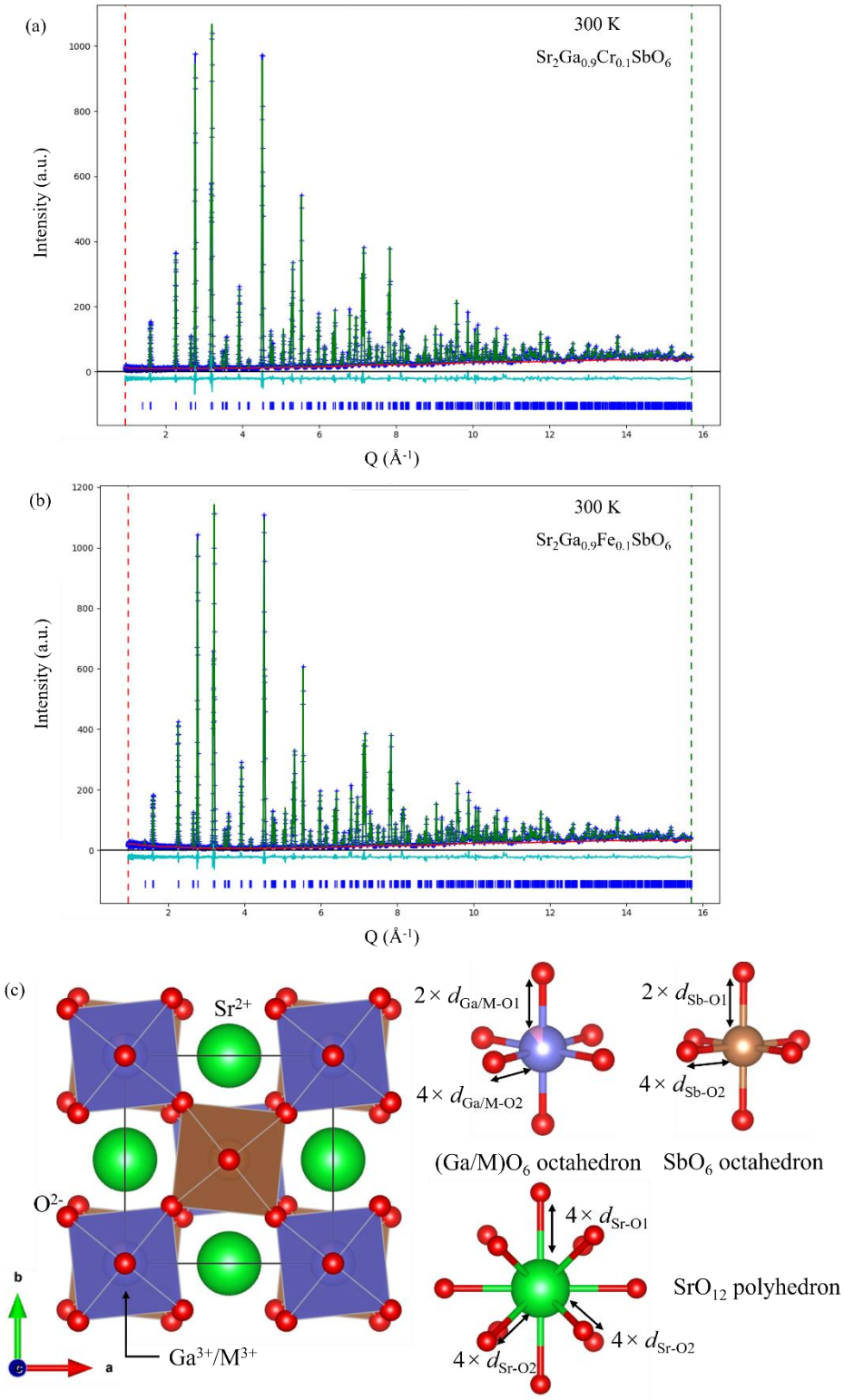

Figure 1. Observed, calculated and difference plots from the Rietveld refinement of (a) $Sr_2Ga_{0.9}Cr_{0.1}SbO_6$ and (b) $Sr_2Ga_{0.9}Fe_{0.1}SbO_6$ (space group *I*4/*m*) against neutron powder diffraction data collected at 300 K; (c) The structural model of $Sr_2Ga_{0.9}M_{0.1}SbO_6$ (M = Cr/Fe), and the selected bonding environment of the $Ga_{0.9}M_{0.1}O_6$ octahedron, SbO_6 octahedron and the SrO_{12} polyhedron.

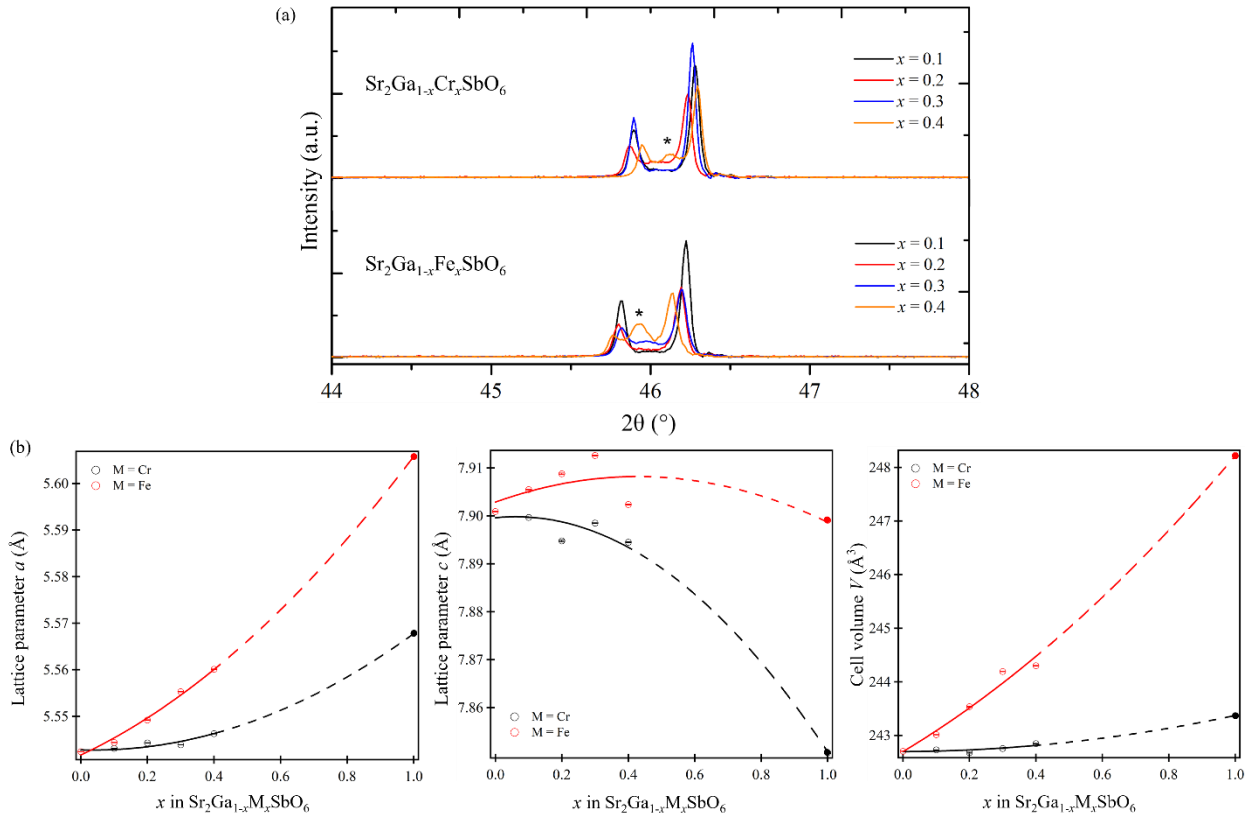

Figure 2. (a) Stacked lab X-ray diffraction patterns for all compositions of the $Sr_2Ga_{1-x}M_xSbO_6$ series (M = Cr/Fe); (b) lattice parameter *a*, *c* and cell volume *V* (open circles) plotted for each composition of $Sr_2Ga_{1-x}M_xSbO_6$ series (M = Cr/Fe). (Data points plotted as closed circles are extracted from literature for the end-members Sr_2CrSbO_6 and Sr_2FeSbO_6.)

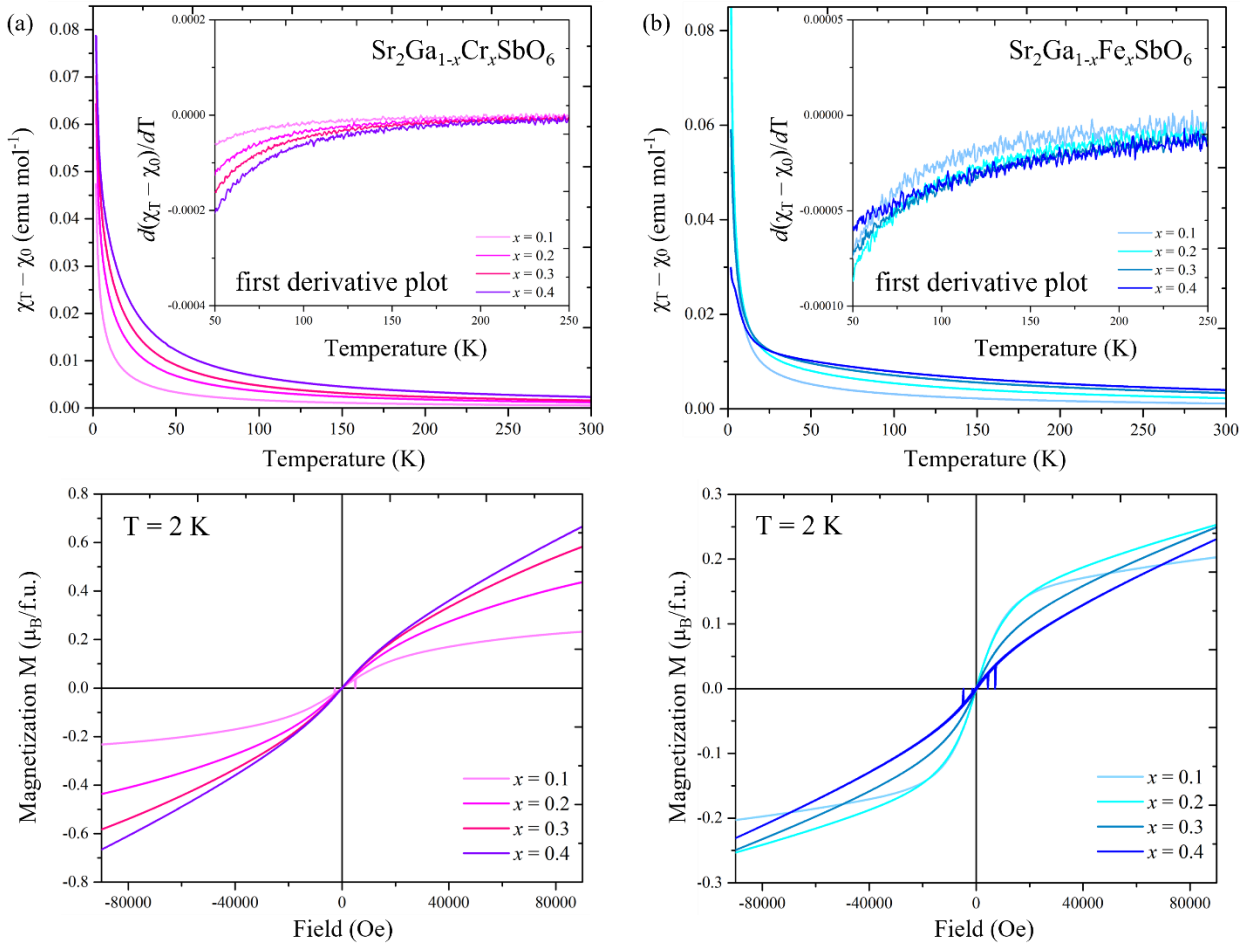

Figure 3. The ($\chi_T - \chi_0$) plotted against temperature, with the first derivative plot embedded (top) and the magnetic moment *M* collected at 2 K plotted against field *H* (bottom) for each composition in the (a) $Sr_2Ga_{1-x}Cr_xSbO_6$ series and (b) $Sr_2Ga_{1-x}Fe_xSbO_6$ series.

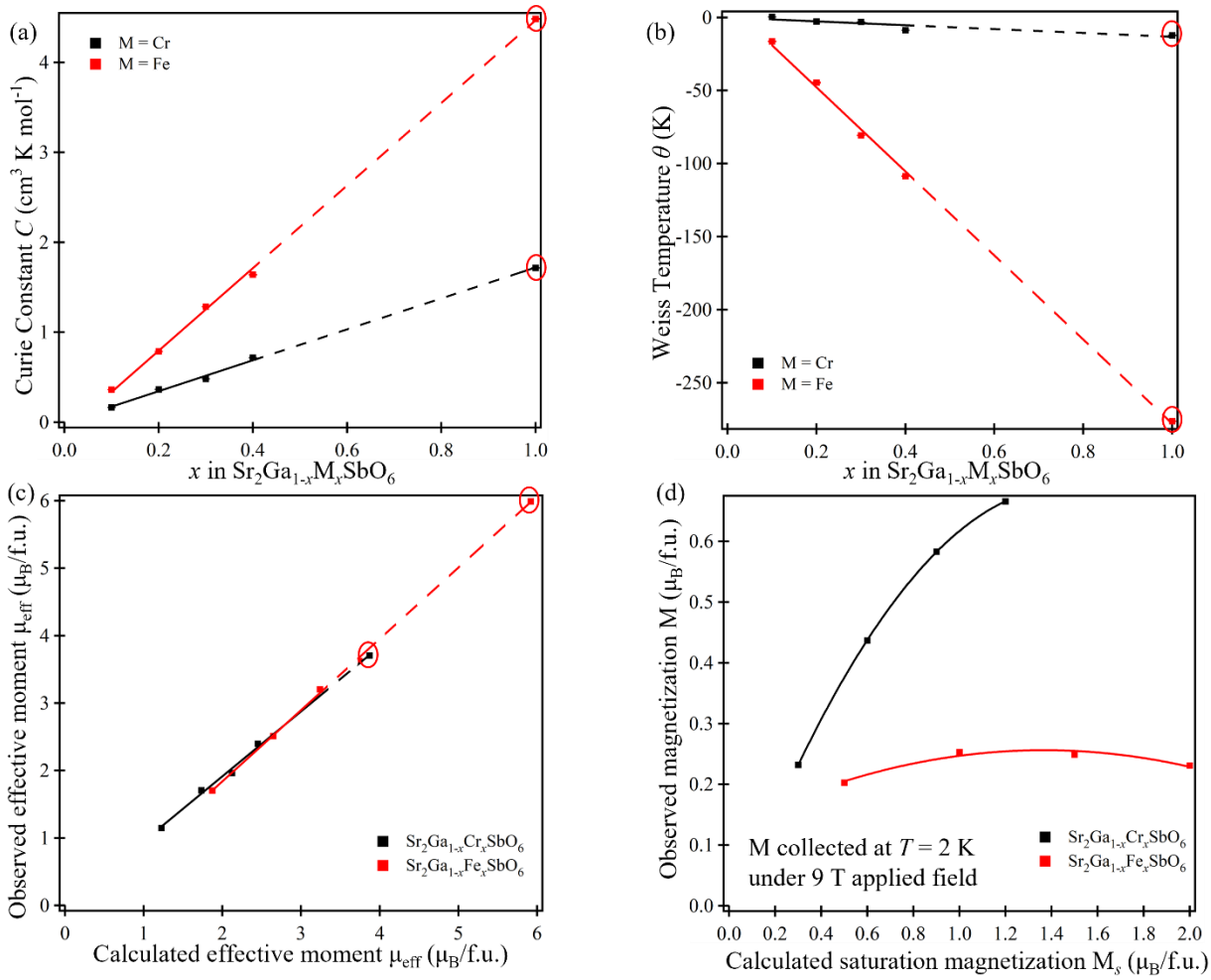

Figure 4. (a) The Curie constant and (b) the Weiss temperature extracted from the fitting of paramagnetic susceptibility to the Curie-Weiss law; (c) the observed effective moment per formula unit plotted against the effective moment per formula unit calculated from the spin-only contribution; (d) the observed magnetization at 2 K under an applied field of 9 T plotted against the calculated saturation magnetization (error bars are smaller than the data points) for each composition of $Sr_2Ga_{1-x}M_xSbO_6$ series (M = Cr/Fe). (Data points in red circles are extracted from literature for the end-members Sr_2CrSbO_6 and Sr_2FeSbO_6, which fall in line with the materials reported here.)

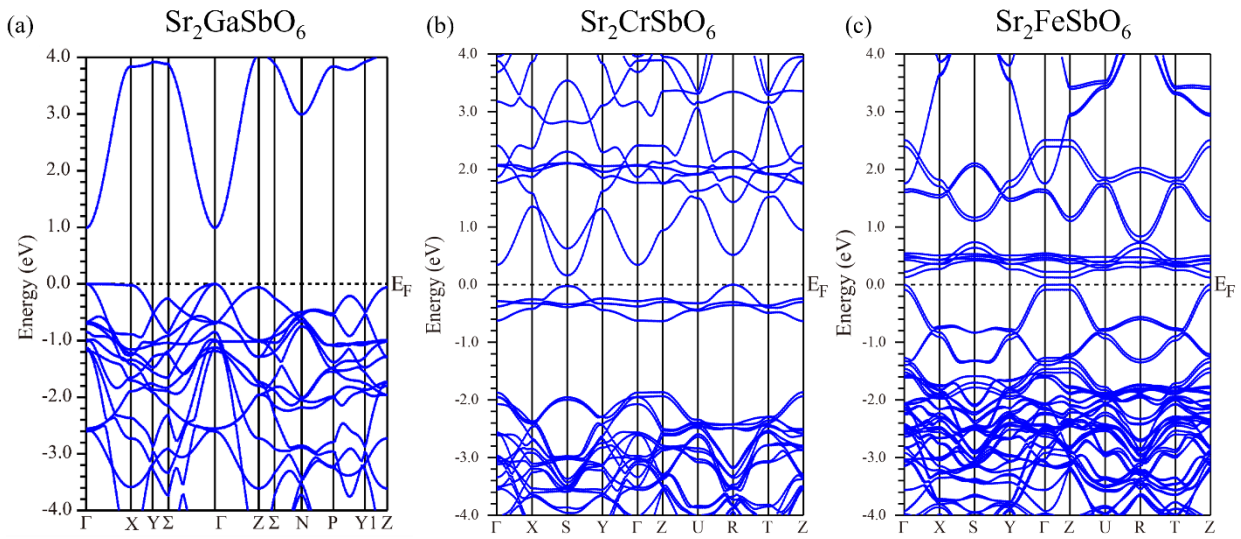

Figure 5. Calculated band structures of (a) Sr_2GaSbO_6, (b) Sr_2CrSbO_6 and (c) Sr_2FeSbO_6.

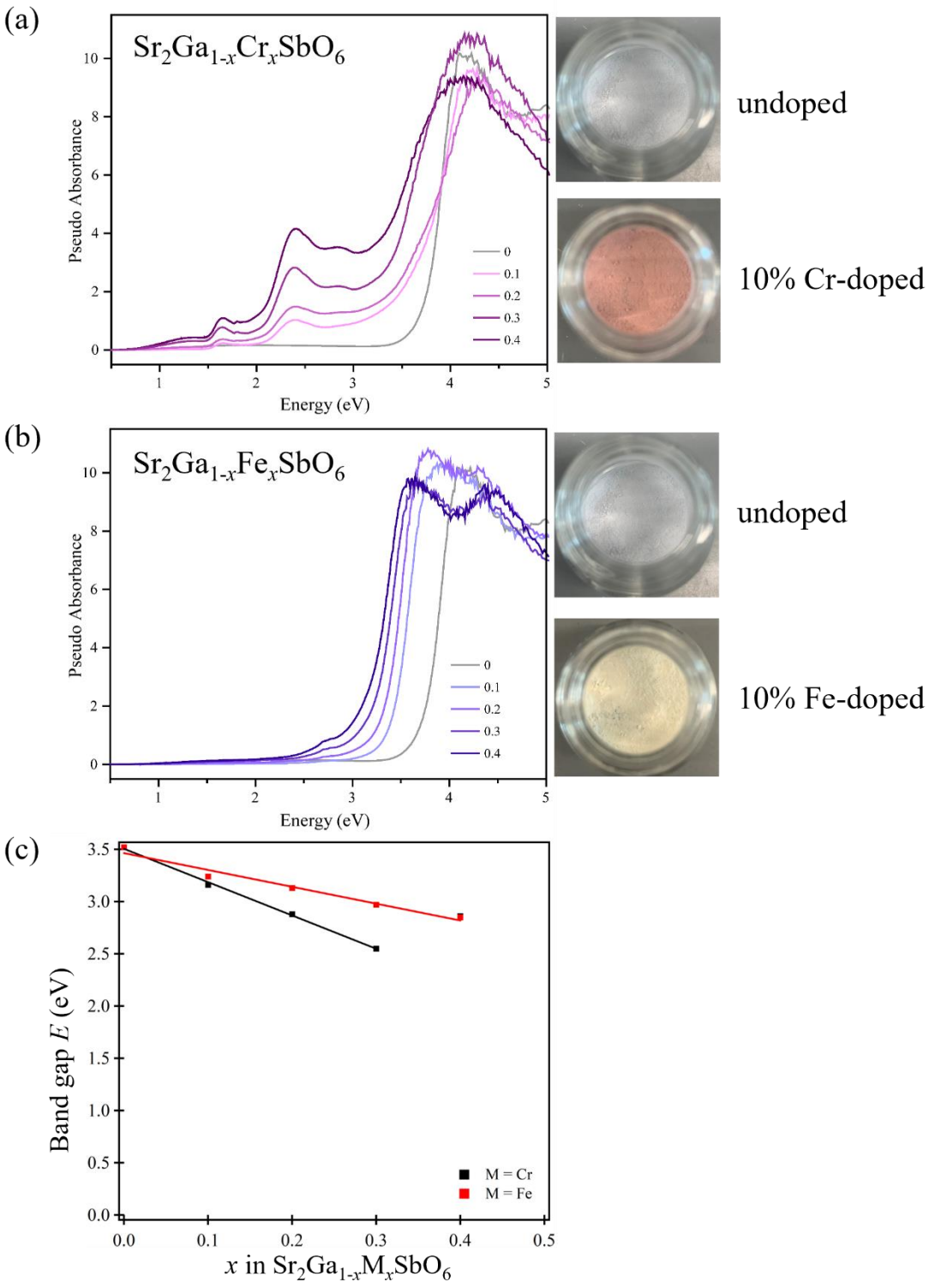

Figure 6. The diffuse reflectance spectra accompanied by the color change for one composition of the (a) $Sr_2Ga_{1-x}Cr_xSbO_6$ series and (b) $Sr_2Ga_{1-x}Fe_xSbO_6$ series; and (c) the band gaps from Tauc plots obtained by using an indirect transition equation plotted against the doping level *x* for both Cr- and Fe-doped series.

References

1 P. Schiffer, A. P. Ramirez, W. Bao and S.-W. Cheong, *Phys. Rev. Lett.*, 1995, **75**, 3336–3339.

2 R. E. Cohen, *Nature*, 1992, **358**, 136.

3 A. H. Macdonald, P. Schiffer and N. Samarth, *Nat. Mater.*, 2005, 4, 195–202.

4 T. Story, R. R. Gafqzka, R. B. Frankel and P. A. Wolff, *Phys. Rev. Lett.*, 1986, **56**, 777–779.

5 T. Dietl and H. Ohno, *MRS Bull.*, 2003, **28**, 714–719.

6 H. Munekata, H. Ohno, ' S Von Molnar, A. Segmuller, L. L. Chang and L. Esaki, *Phys. Rev. Lett.*, 1989, **63**, 1849–1852.

7 T. Dietl, H. Ohno, F. Matsukura, J. Cibert and D. Ferrand, *Science.*, 2000, **287**, 1019–1022.

8 T. Kong, K. Stolze, E. I. Timmons, J. Tao, D. Ni, S. Guo, Z. Yang, R. Prozorov and R. J. Cava, *Adv. Mater*, 2019, **31**, 1808074.

9 T. Dietl, *Semicond. Sci. Technol*, 2002, **17**, 377–392.

10 X. Li and J. Yang, *Natl. Sci. Rev.*, 2016, **3**, 365–381.

11 M.-R. Li, M. Retuerto, Z. Deng, P. W. Stephens, M. Croft, Q. Huang, H. Wu, X. Deng, G. Kotliar, J. Sánchez-Benítez, J. Hadermann, D. Walker and M. Greenblatt, *Angew. Chemie Int. Ed.*, 2015, **54**, 12069–12073.

12 H. Ohno, *Science.*, 1998, **281**, 951–956.

13 J. K. Furdyna, *J. Appl. Phys.*, 1998, **64**, R29.

14 M. A. Pen˜a and J. L. G. Fierro, *Chem. Rev.*, 2001, **101**, 1981–2017.

15 I. Chung, B. Lee, J. He, R. P. H. Chang and M. G. Kanatzidis, *Nature*, 2012, **485**, 486–489.

16 J. Sunarso, S. S. Hashim, N. Zhu and W. Zhou, *Prog. Energy Combust. Sci.*, 2017, **61**, 57–77.

17 S. Vasala and M. Karppinen, *Prog. Solid State Chem.*, 2015, **43**, 1–36.

18 M. T. Anderson, K. B. Greenwood, G. A. Taylor and K. R. Poeppelmeier, *Prog. Solid State Chem.*, 1993, **22**, 197–233.

19 M. W. Lufaso, R. B. MacQuart, Y. Lee, T. Vogt and H. C. Zur Loye, *J. Phys. Condens. Matter*, 2006, **18**, 8761–8780.

20 C. J. Howard, B. J. Kennedy and P. M. Woodward, *Acta Crystallogr. Sect. B*, 2003, **59**, 463–471.

21 M. Cheah, P. J. Saines and B. J. Kennedy, *J. Solid State Chem.*, 2006, **179**, 1775–1781.

22 M. Retuerto, M. García-Hernández, M. J. Martínez-Lope, M. T. Fernández-Díaz, J. P. Attfield and J. A. Alonso, *J. Mater. Chem.*, 2007, **17**, 3555–3561.

23 E. C. Hunter and P. D. Battle, *J. Solid State Chem.*, 2018, **264**, 48–58.

24 S. Baidya and T. Saha-Dasgupta, *Phys. Rev. B*, 2012, **86**, 024440.

25 A. Faik, J. M. Igartua, M. Gateshki and G. J. Cuello, *J. Solid State Chem.*, 2009, **182**, 1717–1725.

26 P. D. Battle, T. C. Gibb, A. J. Herod and J. P. Hodges, *J. Mater. Chem.*, 1995, **5**, 75–78.

27 N. Kashima, K. Inoue, T. Wada and Y. Yamaguchi, *Appl. Phys. A*, 2002, **74**, 805–807.

28 A. Faik, J. M. Igartua, E. Iturbe-Zabalo and G. J. Cuello, *J. Mol. Struct.*, 2010, **963**, 145–152.

29 H. Rietveld, *J. Appl. Crystallogr.*, 1969, **2**, 65–71.

30 A. Y. Tarasova, L. I. Isaenko, V. G. Kesler, V. M. Pashkov, A. P. Yelisseyev, N. M. Denysyuk and O. Y. Khyzhun, *J. Phys. Chem. Solids*, 2012, **73**, 674–682.

31 P. Blaha, K. Schwarz, G. K. H. Madsen, D. Kvasnicka, J. Luitz, R. Laskowsk, F. Tran, L. Marks and L. Marks, *WIEN2k: An Augmented Plane Wave Plus Local Orbitals Program for Calculating Crystal Properties*, Techn. Universitat, 2019.

32 E. Wimmer, H. Krakauer, M. Weinert and A. J. Freeman, *Phys. Rev. B*, 1981, **24**, 864–875.

33 J. P. Perdew and Y. Wang, *Phys. Rev. B*, 1992, **45**, 13244–13249.

34 R. D. King-Smith and D. Vanderbilt, *Phys. Rev. B*, 1993, **47**, 1651–1654.

35 S. Berri, *Chinese J. Phys.*, 2017, **55**, 2476–2483.

36 P. Mori-Sánchez, A. J. Cohen and W. Yang, *Phys. Rev. Lett.*, 2008, **100**, 146401.

37 L. J. Sham and M. SchÏter, *Phys. Rev. Lett.*, 1983, **51**, 1888–1891.

38 J. P. Perdew and M. Levy, *Phys. Rev. Lett.*, 1983, **51**, 1884–1887.

39 J. P. Perdew, W. Yang, K. Burke, Z. Yang, E. K. U. Gross, M. Scheffler, G. E. Scuseria, T. M. Henderson, I. Y. Zhang, A. Ruzsinszky, H. Peng, J. Sun, E. Trushin and A. Görling, *Proc. Natl. Acad. Sci.*, 2017, **114**, 2801–2806.

40 J. P. Perdew, *Int. J. Quantum Chem.*, 1985, **28**, 497–523.

41 R. G. Burns, *Geochim. Cosmochim. Acta*, 1975, **39**, 857–864.

42 D. L. Wood and J. Tauc, *Phys. Rev. B*, 1972, **5**, 3144.

43 B. J. Wood and R. G. J. Strens, *Mineral. Mag.*, 1979, **43**, 509–518.

44 L. Jin, D. Ni, X. Gui, D. B. Straus, Q. Zhang and R. J. Cava, Adv. Sci. 2022, 2104319.